Research Article | Open Access

Catalysis, Energy and Environment

Gao *et al. Catal. Energy Environ.* **2026**, *1*, 4 **DOI:**10.20517/cee.2026.14

Selective ROS-mediated oxidative depolymerization of lignin to guaiacyl monomers over a mesoporous Cu_2Fe_1/JN catalyst

Jie Gao[1], Yingxuan Cai[2], Lu Li[2], Jieting Li[2], Yang Cao[3], Yong Guo[4], Pingyi Zhang[2], Xiang Zheng[1], Linxiang Mo[5], Aijun Zhou[5], Jibo Liu[2,*], Haifang Mao[1,*], Shicheng Zhang[6,7,*]

Keywords:
Lignin valorization, oxygen activation, redox cooperativity, catalytic interfaces, aromatic platform chemicals

Citation: Gao, J.; Cai, Y.; Li, L.; Li, J.; Cao, Y.; Guo, Y.; Zhang, P.; Zheng, X.; Mo, L.; Zhou, A.; Liu, J.; Mao, H.; Zhang, S. Selective ROS-mediated oxidative depolymerization of lignin to guaiacyl monomers over a mesoporous Cu_2Fe_1/JN catalyst. *Catal. Energy Environ.* **2026**, *1*, 4. https://dx.doi.org/10.20517/cee.2026.14

Received: 31 Jul 2026
First Decision: 21 Aug 2026
Revised: 31 Aug 2026
Accepted: 11 Sep 2026
Published: 18 Sep 2026

Academic Editor:
Yongfa Zhu
Copy Editor:
Shu-Yuan Duan
Production Editor:
Shu-Yuan Duan

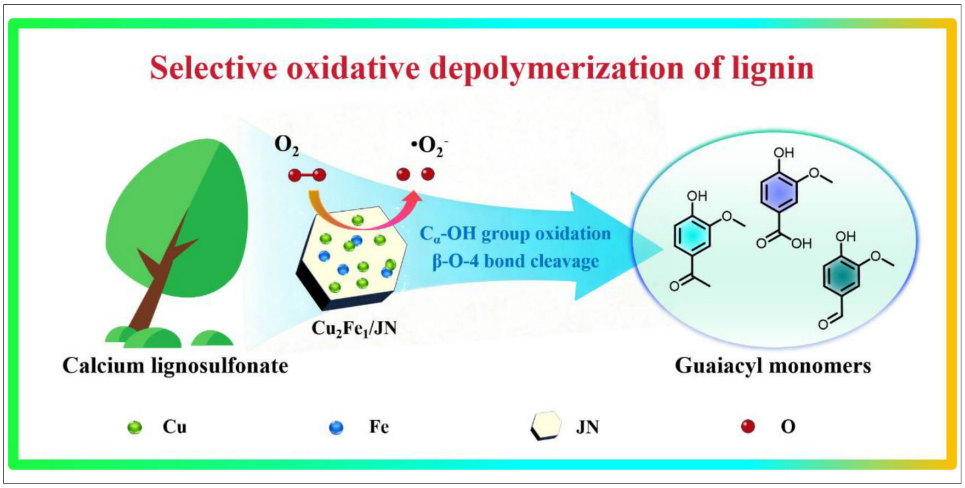

Abstract

Selective oxidative depolymerization of lignin requires precise regulation of reactive oxygen species (ROS) generation. Here, we report a mesoporous silica-supported Cu-Fe catalyst featuring electronically coupled interfacial sites to steer ROS-mediated lignin depolymerization. The optimized Cu_2Fe_1/JN converts calcium lignosulfonate into guaiacyl (G)-type aromatic monomers, achieving 71.8% of the NBO-estimated theoretical yield at 150 °C, far surpassing monometallic catalysts including Cu/JN (46.9%) and Fe/JN (47.6%). Comprehensive radical probing tests, *in situ* spectroscopic characterizations, and theoretical calculations reveal that interfacial electron transfer between the Cu^+/Cu^{2+} and Fe^{2+}/Fe^{3+} redox couples drives O_2 activation to generate $\cdot O_2^-$. The resulting $\cdot O_2^-$ selectively oxidizes the C_α-OH group to a carbonyl intermediate, redistributing electron density to weaken the C_α-C_β and β-O-4 bonds, thereby enabling its selective cleavage into G-monomers. This work reveals the pivotal role of interfacial electronic coupling in directing

[1]Faculty of Flavour Fragrance and Cosmetics, Shanghai Institute of Technology, Shanghai 201418, China.
[2]Faculty of Chemical Engineering and Energy Technology, Shanghai Institute of Technology, Shanghai 201418, China.
[3]College of Engineering, Nanjing Agricultural University, Nanjing 210031, Jiangsu, China.
[4]State Key Laboratory of Green Chemical Engineering and Industrial Catalysis, School of Chemistry and Molecular Engineering, East China University of Science and Technology, Shanghai 200237, China.
[5]Jiaxing Zhonghua Chemical Co., Ltd., Jiaxing 314006, Zhejiang, China.
[6]Shanghai Technical Service Platform for Pollution Control and Resource Utilization of Organic Wastes, Shanghai Key Laboratory of Atmospheric Particle Pollution and Prevention (LAP3), Department of Environmental Science and Engineering, Fudan University, Shanghai 200438, China.
[7]Shanghai Institute of Pollution Control and Ecological Security, Shanghai 200092, China.

*Correspondence to: Dr. Jibo Liu, Faculty of Chemical Engineering and Energy Technology, Shanghai Institute of Technology, 100 Haiquan Road, Shanghai 201418, China. E-mail: jiboliu@sit.edu.cn; Prof. Haifang Mao, Faculty of Flavour Fragrance and Cosmetics, Shanghai Institute of Technology, Shanghai 201418, China. E-mail: mhf@sit.edu.cn; Prof. Shicheng Zhang, Shanghai Technical Service Platform for Pollution Control and Resource Utilization of Organic Wastes, Shanghai Key Laboratory of Atmospheric Particle Pollution and Prevention (LAP3), Department of Environmental Science and Engineering, Fudan University, Shanghai 200438, China; Shanghai Institute of Pollution Control and Ecological Security, Shanghai 200092, China. E-mail: zhangsc@fudan.edu.cn

ROS evolution for selective lignin linkage activation, establishing a general design principle for oxidative lignin valorization.

INTRODUCTION

Lignin is the most abundant renewable aromatic polymer on Earth and represents a sustainable feedstock for the production of value-added aromatic chemicals[1-4]. It contains three monomers of *p*-coumaryl (H), coniferyl (G), and sinapyl (S) alcohols, which are randomly connected through various C-C and C-O bonds[1,5,6]. Selective oxidative cleavage of these linkages provides a promising strategy for lignin depolymerization, enabling the production of value-added aromatic compounds, including vanillin, acetovanillone, vanillic acid, and other derivatives with broad applications in the food, fragrance, pharmaceutical, and fine chemical industries[7,8]. Therefore, developing efficient and selective catalytic oxidation processes for lignin depolymerization is crucial for advancing sustainable biorefining and the renewable production of aromatic chemicals.

The highly delocalized electronic structure and robust aromatic framework of lignin render its C-O and C-C bonds intrinsically resistant to activation[9,10]. Consequently, oxidative depolymerization relies on reactive oxygen species (ROS) generated on catalyst surfaces to promote selective linkage cleavage and functional-group conversion[11]. Alkaline nitrobenzene oxidation (NBO) is widely used as a benchmark to estimate the maximum recoverable aromatic monomer yield from lignin[12,13]. Accordingly, the relative molar yield (RMY) was defined as the ratio of the experimentally obtained yield of monocyclic aromatic products to the corresponding NBO-derived theoretical yield. Therefore, RMY represents the fraction of the theoretically available monocyclic aromatic products that was experimentally recovered from lignin. However, the toxicity of nitrobenzene justifies the development of greener oxidation for lignin valorization[14,15]. Molecular oxygen (O_2) is particularly attractive as a green oxidant[14,16], but its direct involvement in oxidation reactions is kinetically restricted by the high O=O bond dissociation energy and spin-forbidden electronic configuration[14,17]. Efficient O_2 activation to generate ROS, such as superoxide radicals ($\cdot O_2^-$), hydroxyl radicals (·OH), and singlet oxygen ($^1O_2$), is essential for driving lignin depolymerization[17,18]. Among these species, ·OH possesses extremely high oxidation activity and readily induces non-selective oxidation, resulting in the over-oxidation of aromatic monomers into carboxylic acids, as well as aromatic ring opening and even mineralization[14,18,19]. In contrast, the relatively milder $\cdot O_2^-$ preferentially drives selective oxidation through electron- and hydrogen-transfer pathways, enabling controlled cleavage of lignin interunit linkages while preserving aromatic products[20]. Therefore, selective lignin depolymerization depends on precisely regulating the identity, concentration, and reaction pathways of ROS to steer oxidation toward targeted linkage cleavage while suppressing undesired over-oxidation. Despite recent advances, the mechanisms by which catalyst electronic structure governs O_2 activation and ROS evolution remain poorly understood. Achieving precise control over ROS generation and reactivity remains a challenge for selective lignin oxidation.

Engineering bimetallic interfaces with tailored electronic structures offers a promising strategy to regulate O2 activation and direct ROS-mediated oxidation pathways. The electronic coupling between distinct metal centers can modulate charge redistribution, facilitate redox cycling, and regulate the formation and evolution

of ROS[21]. Among various bimetallic systems, Cu-Fe interfaces are particularly promising because the Cu^{+}/Cu^{2+} redox cycle enables efficient electron transfer to O_2, while Fe species provide Lewis acidic sites and ROS-generation capability[22,23]. For instance, a Fe-Cu bimetallic catalyst supported on ZSM-5 zeolite enabled the selective production of formic acid (up to 80.3% selectivity at 40 °C) through Fenton-type oxidation of guaiacol and other lignin-derived compounds[24]. However, the realization of Cu-Fe synergistic interactions relies on a suitable support capable of regulating the spatial distribution and coordination environment of the metal centers[22]. Mesoporous SiO_2 derived from JN30 ion-exchanged silica sol represents an ideal platform for this purpose owing to its high surface area, structural stability, and tunable mesoporous architecture. It can anchor Cu and Fe species and facilitate the formation of accessible interfacial active sites[25,26]. Such a confined interfacial environment is expected to promote electronic communication between Cu and Fe centers, enabling regulated O_2 activation and ROS evolution for selective lignin oxidation.

Herein, we construct a mesoporous silica-supported Cu-Fe bimetallic catalyst (Cu_2Fe_1/JN) for oxygen-driven selective oxidative depolymerization of calcium lignosulfonate. The mesoporous JN support stabilizes highly dispersed Cu-Fe active sites while promoting interfacial electronic coupling. Benefiting from the synergistic interaction between Cu and Fe sites, Cu_2Fe_1/JN facilitates the selective conversion of calcium lignosulfonate into value-added aromatic monomers under mild reaction conditions. Combined radical scavenging tests, electron paramagnetic resonance spectroscopy, *in situ* spectroscopic characterization, and theoretical calculations reveal the mechanistic pathway involving the generation of $\cdot O_2^-$ radicals and their critical role in promoting C_α-OH oxidation and β-O-4 bond cleavage.

EXPERIMENTAL

Synthesis and characterization of Cu_2Fe_1/JN

Cu_2Fe_1/JN was synthesized *by co-precipitation*. Typically, 30 g of JN30 silica sol (30 wt.% SiO_2) was used as the support precursor. Aqueous solutions of $Cu(NO_3)_2{\cdot}3H_2O$ and $Fe(NO_3)_3{\cdot}9H_2O$ were added dropwise to the silica sol at 300 rpm for 60 min at room temperature. The pH of the suspension was gradually adjusted to 8-10 using 1 M NaOH and maintained under stirring at 300 rpm for 30 min to facilitate the precipitation and uniform dispersion of Cu and Fe species. The resulting precipitate was collected by filtration, dried in a vacuum oven at 110 °C for 12 h, and then calcined in air at 500 °C for 4 h with a heating rate of 5 °C/min. After cooling to room temperature, the Cu_2Fe_1/JN was obtained. To investigate the effect of Cu/Fe mass ratio on catalytic performance, a series of Cu-Fe catalysts with a fixed total metal loading of 20 wt% were synthesized using the same procedure, including Cu/JN, Cu_1Fe_1/JN, Cu_1Fe_2/JN, and Fe/JN with Cu/Fe mass ratios of 1:0, 1:1, 1:2, and 0:1, respectively. To verify the synergistic effect between Cu and Fe, a physical mixture of Cu/JN and Fe/JN with a Cu/Fe mass ratio of 2:1, corresponding to that of Cu_2Fe_1/JN, was also prepared as a control and evaluated under identical reaction conditions. Detailed materials information is provided in the Supplementary Materials (section 1.1).

To elucidate the surface morphology, porous structure, crystalline phases, Cu valence distribution, elemental composition, reducibility, and surface acidity, Cu_2Fe_1/JN was systematically characterized using transmission electron microscopy (TEM) coupled with energy-dispersive X-ray spectroscopy (EDS) elemental mapping, scanning electron microscopy (SEM), N_2 adsorption-desorption analysis (BET), X-ray diffraction (XRD), and X-ray photoelectron spectroscopy (XPS), inductively coupled plasma optical emission spectroscopy (ICP-OES), H_2 temperature-programmed reduction (H_2-TPR), and NH_3 temperature-programmed desorption (NH_3-TPD). Detailed information is provided in the Supplementary Materials (Section 1.2).

Catalytic reactions and analysis of products

Calcium lignosulfonate was used as the substrate because of its well-defined structure and commercial availability[27]. In a typical oxidation reaction, calcium lignosulfonate (2.5 g), Cu_2Fe_1/JN (0.25 g), and NaOH solution (50 mL, 1.25 M) were loaded into a 150 mL stainless-steel high-pressure reactor (YZPR

Micro-reactor, YAN ZHEN INSTRUMENT Co., Ltd.). Prior to the reaction, the reactor was purged with O_2 three times to remove residual air. The reactor was then heated to 150 °C at 500 rpm, followed by charging with 0.4 MPa O_2 to initiate the reaction. The reaction was subsequently conducted under a constant O_2 atmosphere for the required time. The theoretical yield of lignin-derived monomeric aromatics was estimated by nitrobenzene oxidation (NBO). Briefly, calcium lignosulfonate (0.15 g), NaOH solution (38 mL, 2 M), and nitrobenzene (2 mL) were reacted at 170 °C for 3 h at 500 rpm. The reaction products were identified by gas chromatography-mass spectrometry (GC-MS) and quantified by high-performance liquid chromatography (HPLC). To assess the effect of the mesoporous structure on substrate accessibility and mass transfer, the concentration of 2-phenoxy-1-phenylethanol remaining in the liquid phase was monitored under otherwise identical reaction conditions but in the absence of high-pressure O_2 (Supplementary Materials, Section 1.3). Catalyst recyclability was assessed by recovering and reusing the Cu_2Fe_1/JN after each cycle, with detailed procedures provided in the Supplementary Materials (Section 1.4). All experiments were conducted in triplicate, and the error bars represent the standard deviation (SD) of the three independent measurements, reflecting the variability among experimental replicates. The relative G-derived aromatic monomers yield (RGY) was defined as the ratio of the experimentally obtained G-derived aromatic monomers yield to the corresponding theoretical yield obtained by the NBO method[27]. Thus, RGY represents the fraction of the theoretically available G-monomer that was experimentally recovered from lignin. Detailed post-reaction procedures and yield calculations are available in the Supplementary Materials (Section 1.5).

Detection of ROS

The generation of ROS was monitored by *in situ* UV-vis spectroscopy using 3,3′,5,5′-tetramethylbenzidine (TMB) as a chromogenic probe. The UV-vis spectra were continuously recorded at predetermined intervals over the range of 350-700 nm to track the formation of ROS-derived oxidation products. ROS species were further identified by electron paramagnetic resonance (EPR) spectroscopy using 5,5'-dimethyl-1-pyrroline *N*-oxide (DMPO) and 2,2,6,6-tetramethylpiperidine-1-oxyl (TEMPO) as spin-trapping agents. To further correlate ROS generation with catalytic oxidation, 1-phenylethanol and 2-phenoxy-1-phenylethanol were employed as model substrates. Moreover, radical scavenging experiments were performed using selective quenchers, including *p*-benzoquinone for superoxide radicals ($\cdot O_2^-$), β-carotene for singlet oxygen ($^1O_2$), and isopropanol for hydroxyl radicals (·OH), to evaluate the contribution of individual ROS species during the reaction. Detailed descriptions can be accessed in Supplementary Materials (Section 1.6).

Lignin structure characterization

To elucidate the correlation between lignin structure and product distribution, both native and residual lignin samples were characterized by Fourier-transform infrared (FTIR) spectroscopy. The structural evolution of lignin during depolymerization was further monitored in real time using *in situ* UV-vis and *in situ* FTIR spectroscopy. Note that the 2D contour plot of UV-vis spectra represents non-continuously sampled data points and is intended only to illustrate the temporal evolution of the absorption peaks, rather than to indicate a continuous spectral distribution. Detailed information is presented in Supplementary Materials (Section 1.7).

Density functional theory calculations

The geometries of lignin model compounds and representative intermediates generated during depolymerization were optimized using Gaussian 16 at the B3LYP/6-31G level. Molecular electrostatic potential (MEPS) surfaces were subsequently calculated using the Multiwfn program and visualized with VMD. Bond dissociation energies (BDEs) were calculated using Gaussian 16 at the B3LYP/6-31G level of

theory[28]. Geometries of the parent molecule and the corresponding dissociated radical fragments were fully optimized without symmetry constraints. Then, vibrational frequency calculations were performed for all optimized structures to confirm that each stationary point is a local minimum (no imaginary frequencies). When evaluating energies, zero-point vibrational energy (ZPVE) corrections obtained from frequency analysis were included.

RESULTS AND DISCUSSION

Physicochemical properties of Cu_2Fe_1/JN

The morphology of Cu_2Fe_1/JN was first characterized by SEM and TEM. As shown in Figure 1A-E and Supplementary Figure 1A-H, Cu_2Fe_1/JN and Fe/JN exhibit a rough and irregular surface uniformly decorated with nanoparticles. In contrast, obvious Cu nanoparticle aggregation is observed in Cu/JN [Supplementary Figure 2A-H]. These observations indicate that Fe incorporation effectively suppresses Cu aggregation and promotes the formation of highly dispersed metal species. ICP-OES analysis shows that the actual Cu and Fe loadings are close to the designed values [Supplementary Table 1], confirming the successful incorporation of both metal species into the JN support. Moreover, the textural properties were analyzed by N_2 adsorption-desorption isotherms [Figure 1F]. JN exhibits a typical type-IV isotherm with an H4 hysteresis loop and a mesopore size distribution in the range of 2-10 nm. In contrast, Cu_2Fe_1/JN retains the type-IV isotherm but displays an H2 hysteresis loop, accompanied by enhanced N_2 uptake at a relative pressure (P/P_0) of 0.4-0.8, suggesting a more uniform mesoporous framework with a narrower pore size distribution. However, the specific surface area and pore volume of Cu_2Fe_1/JN decreased from 193.4 to 169.3 m^2/g and from 0.50 to 0.40 cm^3/g, respectively, mainly due to the partial occupation of pore channels by Cu-Fe species[29]. Importantly, Cu_2Fe_1/JN maintains a well-developed mesoporous network, providing interconnected transport pathways and accessible pore environments for lignin-derived substrates and intermediates[30]. Thus, despite the moderate loss of surface area and pore volume upon Cu-Fe incorporation, the preserved mesoporosity is expected to facilitate reactant diffusion and promote access to the Cu-Fe active sites.

The structural features of Cu_2Fe_1/JN were further elucidated by XRD analysis. The broad diffraction band centered at 21.98° is assigned to amorphous SiO_2 (PDF No. 29-0085) derived from the JN support [Figure 1G]. For Cu/JN, the diffraction peaks at 32.51°, 35.54°, 38.90°, 48.72°, 53.49°, 58.34°, 61.54°, 66.25°, 68.09°, 72.43°, and 75.23° correspond to the monoclinic CuO phase (PDF No. 45-0937), confirming the formation of crystalline CuO species. In contrast, the absence of diffraction peaks in Fe/JN suggests well-dispersed Fe species on JN. Notably, the characteristic CuO peaks in Cu_2Fe_1/JN become markedly weaker after Fe incorporation, indicating inhibited CuO crystallization and enhanced Cu dispersion. This structural modulation is likely associated with the interaction between Cu and Fe species, which inhibits Cu migration and aggregation during calcination[31]. The existence of CuO species is consistent with HRTEM analysis, where lattice fringes corresponding to the CuO (111) plane were observed [Figure 1D]. Given the structural modulation induced by Cu-Fe incorporation, the interfacial electronic interactions in Cu_2Fe_1/JN were subsequently investigated by XPS. As shown in Figure 1H-I, the Cu 2p peaks of Cu_2Fe_1/JN shift toward lower binding energies compared with those of Cu/JN, whereas the Fe 2p peaks exhibit a positive shift relative to Fe/JN. These opposite shifts indicate the electron transfer from Fe to Cu. Consistent with this electronic redistribution, the Cu^+ fraction increased from 60.3% in Cu/JN to 62.7% in Cu_2Fe_1/JN, accompanied by a decrease in the Fe^{2+} fraction from 54.6% in Fe/JN to 52.6% in Cu_2Fe_1/JN upon Cu-Fe incorporation [Supplementary Tables 2 and 3]. The concurrent enrichment of Cu^+ and Fe^{3+} species indicates that Cu-Fe coupling modifies the local redox environment, favoring the Cu^+/Cu^{2+} and Fe^{2+}/Fe^{3+} redox couples and providing a favorable basis for interfacial redox cycling[32]. The modified electronic structure further affects the surface oxygen chemistry. The O 1s spectra can be deconvoluted into three oxygen species, including lattice oxygen (O_{latt}, 529.5 eV), oxygen near vacancies or surface defect oxygen (O_{vac}, 531.5 eV), and surface-adsorbed oxygen species (O_{ads}, 532.7 eV)[33]. Compared with Cu/JN and Fe/JN, Cu_2Fe_1/JN exhibited a

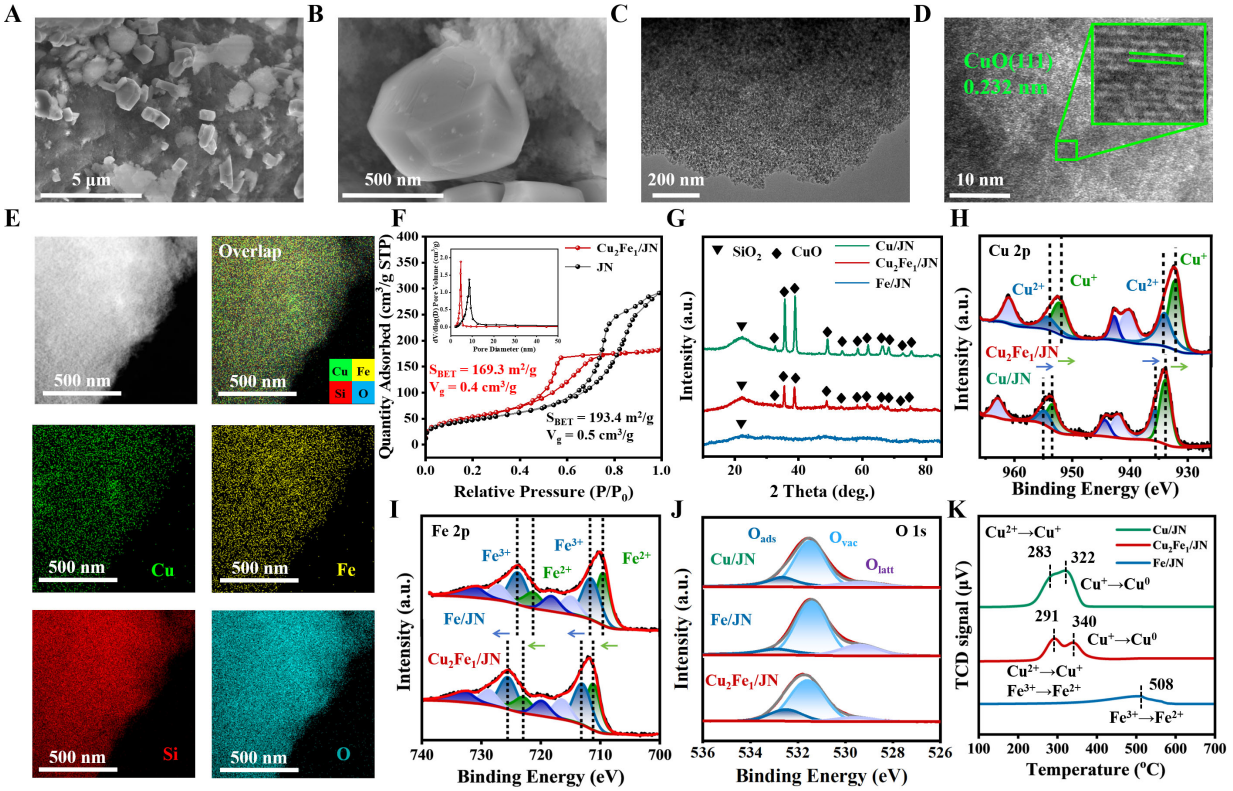

Figure 1. Morphology and surface chemical property analysis of Cu_2Fe_1/JN. (A and B) SEM images; (C and D) TEM images; (E) Corresponding energy-dispersive X-ray spectroscopy (EDS) elemental mapping of the overlapped image and Cu, Fe, Si, and O elements; (F) Nitrogen adsorption-desorption isotherm and the corresponding pore size distributions (inset); (G) XRD pattern; (H-J) High-resolution XPS spectra of Cu 2p, Fe 2p, and O 1s; (K) H_2-TPR profiles. SEM: Scanning electron microscopy; TEM: transmission electron microscopy; XRD: X-ray diffraction; XPS: X-ray photoelectron spectroscopy; H_2-TPR: H_2 temperature-programmed reduction.

markedly higher O_{ads} fraction (19.9%) [Figure 1J and Supplementary Table 4]. This enrichment of surface-adsorbed oxygen species suggests that Fe incorporation modulates the surface oxygen environment to facilitate O_2 adsorption and activation, thereby favoring sustained ROS generation during subsequent oxidation[34]. As such, electronic interactions are expected to modulate the redox properties of the active species; H_2-TPR was performed to further evaluate the effect of Cu-Fe coupling on catalyst reducibility. As shown in Figure 1K, Cu/JN exhibits two reduction peaks at 283 and 322 °C, corresponding to the stepwise reduction of CuO to Cu_2O and subsequently to Cu^0[35]. In contrast, Fe/JN displays a broad reduction peak centered at approximately 508 °C, which is assigned to the reduction of dispersed FeO_x species[36,37]. Upon Fe incorporation, the CuO_x reduction peaks appear at higher temperatures (291 and 340 °C), indicating stronger Cu-Fe interactions and enhanced structural stability of Cu species. As shown in Supplementary Figure 3A and B, the surface acidity of Cu_2Fe_1/JN was further evaluated by NH_3-TPD. The three catalysts exhibited comparable densities of weak- and strong-acid sites, with the former remaining at approximately 0.3 mmol/g and the latter varying only slightly from 0.3 to 0.5 mmol/g. These results indicate that surface acidity is unlikely to be the primary factor responsible for the enhanced catalytic performance of Cu_2Fe_1/JN. Collectively, these results show that Cu-Fe incorporation modulates the electronic structure and redox properties of the metal centers, thereby creating a distinct interfacial environment conducive to redox cycling and O_2 activation.

Catalytic oxidation of calcium lignosulfonate over Cu_2Fe_1/JN

To estimate the maximum achievable yield of aromatic monomers, NBO analysis was first performed, revealing that G-type monomers were the predominant products expected from selective linkage cleavage [Supplementary Table 5]. Accordingly, the recovered RGY was defined as the ratio of experimentally

achieved G-type monomers to the theoretical amount obtainable from the starting lignin, and was used as the primary metric for evaluating catalytic performance[27,38]. The effect of support on catalytic performance was subsequently investigated.

As shown in Figure 2A, Cu_2Fe_1/JN exhibited the highest RGY among the tested catalysts, increasing from 33.8% in the catalyst-free system to 71.8%. Notably, Cu_2Fe_1/JN also delivered a high G-type product yield compared with most previously reported catalysts [Figure 2B and Supplementary Table 6]. Taken together, these results demonstrate the excellent catalytic performance of Cu_2Fe_1/JN. By contrast, Cu-Fe species supported on TiO_2 and C_3N_4 achieved only 42.9%, and 48.7% recovery, respectively. To further distinguish the contribution of the support pore architecture from that of the metal species, Cu-Fe supported on commercial SiO_2 was evaluated [Figure 2A]. Although the Cu and Fe compositions were comparable, Cu_2Fe_1/SiO_2 gave only 44.1% recovery, highlighting the critical role of the mesoporous JN support in promoting catalytic oxidation. To further elucidate the contribution of the mesoporous structure to substrate accessibility, the time-dependent substrate adsorption of 2-phenoxy-1-phenylethanol was investigated under comparable conditions [Supplementary Figures 4 and 5]. The substrate mass decreased rapidly from 0.21 to 0.18 g during the initial stage and then declined more gradually, whereas negligible substrate loss occurred in the catalyst-free control. The pronounced initial decrease suggests facilitated substrate transport within the mesoporous network, promoting access to the Cu-Fe active sites. Together with the catalytic results, these observations highlight the complementary roles of the mesoporous JN framework in facilitating substrate transport and the strong metal-support interaction in stabilizing highly dispersed Cu-Fe species. These combined structural advantages may contribute to the superior performance of Cu_2Fe_1/JN. It is noteworthy that the calcium lignosulfonate used herein was derived from industrial softwood in Norway and exhibits a relatively homogeneous, guaiacyl(G)-rich architecture with a considerable fraction of cleavable β-O-4 bonds[27]. Consequently, oxidative depolymerization generated a well-defined aromatic monomer distribution dominated by vanillin, vanillic acid, and acetovanillone. This simplified product profile, in contrast to that typically obtained from structurally heterogeneous technical lignins, is consistent with the G-rich nature of softwood lignin and demonstrates the high selectivity of Cu_2Fe_1/JN toward G-derived monomers. To identify the optimal Cu/Fe ratio and elucidate the contribution of Cu-Fe interfacial coupling, catalysts with different Cu/Fe mass ratios were systematically evaluated [Figure 2C]. The Cu/Fe mass ratio of 2:1 exhibited the highest activity, delivering a G-monomer yield of 10.4%, corresponding to an RGY of 71.8%. This catalyst markedly outperformed Cu/JN, which gave a G-monomer yield of 6.8% (RGY, 46.9%). Further increasing the Fe content to Cu/Fe ratios of 1:1 and 1:2 progressively decreased the G-monomer yield to 9.2% and 8.9%, respectively, while Fe/JN gave the lowest yield of 6.9% (RGY, 47.6%). The decline in activity at higher Fe contents is probably associated with a reduced abundance of Cu-rich Cu-Fe interfacial ensembles and an increasingly Fe-rich surface, which may limit the redox functionality of the Cu-Fe species. Importantly, a physical mixture of Cu/JN and Fe/JN at the same 2:1 Cu/Fe mass ratio afforded only 7.0% G-monomer yield, substantially lower than that of Cu_2Fe_1/JN. This marked activity gap rules out a simple metal-loading effect and instead highlights the synergistic contribution from the Cu-Fe species. Combined with the XPS and H_2-TPR results, these catalytic data indicate that the optimal 2:1 composition strikes a favorable balance between Cu and Fe, creating an interfacial electronic and redox environment conducive to efficient oxidation.

To further elucidate the oxidative depolymerization of calcium lignosulfonate over Cu_2Fe_1/JN, the effects of reaction temperature, reaction time, NaOH concentration, and O_2 pressure were systematically investigated [Figure 2D-G]. Increasing the reaction temperature from 120 to 150 °C markedly enhanced the G-type monomer recovery from 56.2% to 71.8%, accompanied by an increase in vanillin yield from 5.5% to 7.0% [Figure 2D], indicating more efficient cleavage of interunit linkages in calcium lignosulfonate. However, further increasing the temperature to 180 °C substantially decreased the yields of vanillin, vanillic acid, and

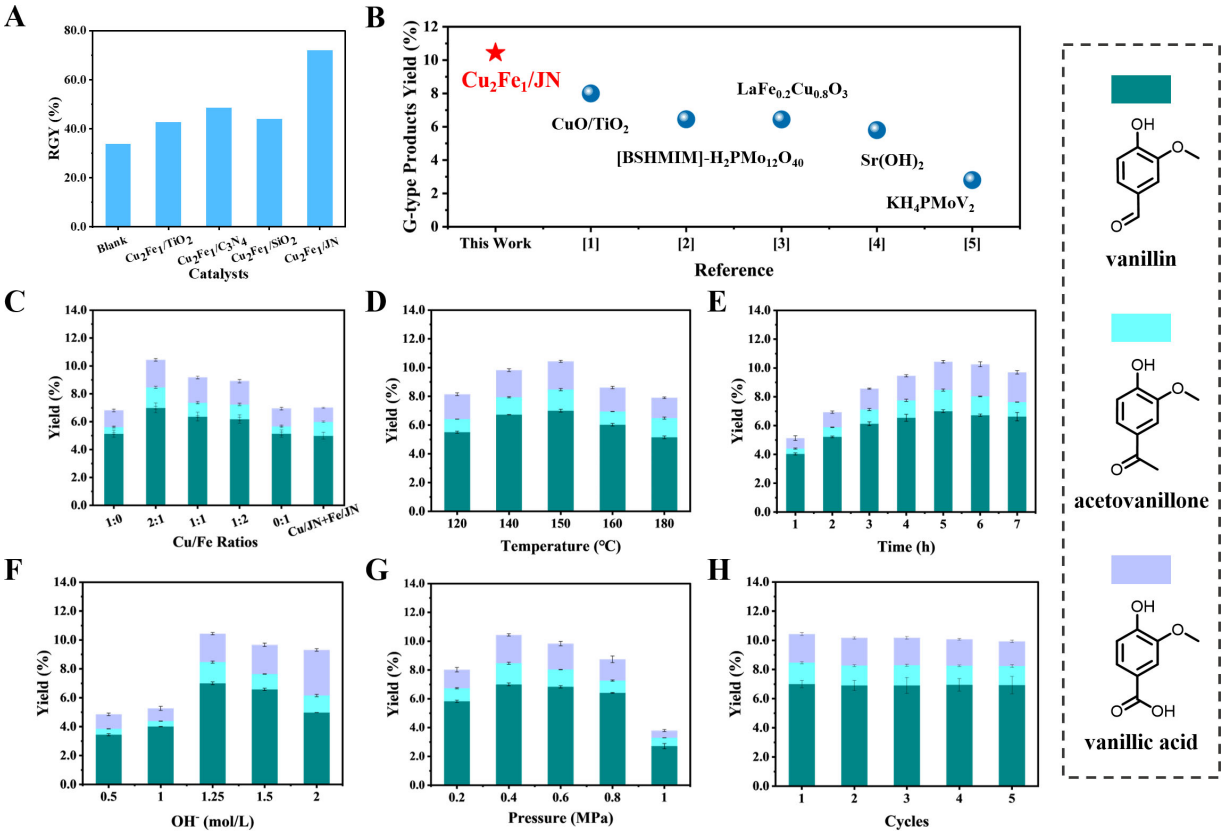

Figure 2. Catalytic performance of Cu_2Fe_1/JN for the oxidative depolymerization of calcium lignosulfonate. (A) Comparison of the catalytic performance of the blank and Cu-Fe catalysts supported on different supports for the oxidative depolymerization of calcium lignosulfonate; (B) Comparison of lignin oxidative depolymerization performance with previously reported catalysts (data from Supplementary Table 6); (C-G) Effect of Cu/Fe ratios, temperature, time, NaOH concentration, and O_2 pressure on calcium lignosulfonate depolymerization; (H) Reusability of Cu_2Fe_1/JN. Reaction conditions: 2.5 g calcium lignosulfonate, 0.25 g Cu_2Fe_1/JN, NaOH solution (50 mL, 1.25 M), 0.4 MPa O_2, 150 °C, 5 h. Data are reported as mean ± standard deviation (N = 3).

acetovanillone to 5.2%, 1.4%, and 1.3%, respectively, along with a decline in G-type monomer recovery to 54.5%. These results suggest that excessive temperatures may induce over-oxidation or secondary degradation of aromatic monomers, which has been frequently observed in lignin oxidation systems[39]. A similar trend was observed with reaction time [Figure 2E]. Extending the reaction time from 1 to 5 h continuously increased the total aromatic monomer yield from 5.1% to 10.4%, whereas prolonging the reaction to 7 h led to lower yields of vanillin (6.6%), vanillic acid (2.1%), and acetovanillone (1.0%) [Supplementary Table 7]. This decline suggests that prolonged reaction time may induce secondary conversion of the generated aromatic monomers, as further evidenced by the *in situ* spectroscopic analysis. The alkaline environment also played a critical role in lignin depolymerization [Figure 2F]. Increasing the NaOH concentration to 1.25 M achieved the highest total aromatic monomer yield and G-type monomer recovery. This enhancement can be attributed to improved solubility of calcium lignosulfonate arising from the deprotonation of phenolic hydroxyl groups, which facilitates the oxidative cleavage of ether bonds[40,41]. Further increasing the NaOH concentration to 2.0 M altered the product distribution, decreasing the vanillin yield to 5.0% while increasing the vanillic acid yield to 3.1%, consistent with previous reports that excessive OH^- facilitates the oxidation of aromatic aldehydes to the corresponding carboxylic acids[42-44]. Moreover, O_2 pressure exerted the greatest influence on product distribution. Raising the O_2 pressure from 0 to 0.4 MPa increased the total aromatic monomer yield from 0.3% to 10.4%, whereas a further increase to 1.0 MPa sharply decreased the yield to 3.8% [Figure 2G and Supplementary Table 7]. This strong dependence on O_2 suggests that it regulates the balance between ROS-mediated lignin depolymerization and over-oxidation of

the aromatic monomers[45-47]. Therefore, elucidating the generation and function of ROS is essential for understanding the oxidation mechanism of the Cu_2Fe_1/JN catalytic system. It can be noticed that the yield of G-type monomers remained nearly unchanged over five cycles, indicating the excellent recyclability of the catalyst [Figure 2H]. The spent Cu_2Fe_1/JN was characterized by XRD and ICP-OES. The characteristic diffraction peaks of CuO were well preserved [Supplementary Figure 6], while the Cu and Fe loadings on JN remained at 11.9 and 6.5 wt.%, respectively [Supplementary Table 1], indicating the high structural stability of the catalyst during recycling. Notably, the Si concentration in the liquid phase was only 0.2 g/L, further highlighting the stability of the JN support under the reaction conditions. Furthermore, the universal catalytic efficiency of Cu_2Fe_1/JN toward structurally diverse lignin feedstocks was evaluated using organosolv and kraft lignins. As shown in Supplementary Figure 7, the total monomer yield reached 15.5% for organosolv lignin, with guaiacol, vanillin, and vanillic acid as the dominant aromatic products. Kraft lignin afforded a total aromatic monomer yield of 9.4%, which may be attributed to its more condensed structure[48]. Overall, Cu_2Fe_1/JN exhibited broad catalytic applicability toward different lignin feedstocks, highlighting its potential for lignin valorization.

Mechanistic insights into ROS-mediated oxidative depolymerization

To gain mechanistic insight into calcium lignosulfonate oxidative depolymerization over Cu_2Fe_1/JN, the generation and role of ROS were first investigated. TMB was employed as a chromogenic probe because its oxidation by ROS produces a blue diimine species, allowing the evolution of ROS to be monitored by UV-vis spectroscopy[49]. As shown in Figure 3A, the characteristic absorption bands at 366, 485, and 656 nm progressively increased with reaction time, indicating sustained ROS generation during O_2 activation over Cu_2Fe_1/JN. Notably, Cu_2Fe_1/JN exhibited a substantially stronger TMB response than Cu/JN and Fe/JN, demonstrating its superior ROS-generating capability and highlighting the promotional effect of Cu-Fe coupling [Supplementary Figures 8 and 9]. Together with the higher O_{ads} fraction observed by XPS, these results support the role of Cu-Fe synergy in facilitating O_2 adsorption and activation and thereby promoting ROS generation. EPR spectroscopy using DMPO as the spin-trapping agent further identified the generated ROS species. The characteristic six-line EPR signal corresponding to DMPO-·O_2^- confirmed the formation of ·O_2^- during the catalytic process [Figure 3B][50]. The specific contribution of ·O_2^- was subsequently evaluated through radical scavenging experiments using 2-phenoxy-1-phenylethanol, a representative β-O-4 lignin model compound. In the absence of scavengers, the reaction achieved nearly complete conversion (99.1%), affording benzaldehyde and benzoic acid in yields of 56.3% and 32.0%, respectively [Table 1]. The introduction of *p*-benzoquinone, a selective ·O_2^- quencher, substantially suppressed the conversion to 56.1%, while the yields of benzaldehyde and benzoic acid dropped to 18.4% and 10.0%, respectively. In contrast, scavenging ·OH with isopropanol or $^1O_2$ with β-carotene produced only negligible effects on either substrate conversion or product yields. These results identify ·O_2^- as the predominant ROS involved in substrate oxidation. The preferential formation of ·O_2^- on Cu_2Fe_1/JN is likely derived from synergistic redox interactions between Cu and Fe species. The optimized Cu-Fe redox cycle enhances O_2 activation by facilitating O_2 adsorption and accelerating interfacial electron transfer, thereby favoring the one-electron reduction of O_2 to ·O_2^-[22,24].

Considering that oxidation of the C_α-OH group into a carbonyl intermediate is generally recognized as the key initiating step for β-O-4 bond cleavage[51], MEPS calculations were performed to clarify the preferred oxidation site in the Cu_2Fe_1/JN system. Using 2-phenoxy-1-phenylethanol and its oxidized counterpart 2-phenoxy-1-phenylethanone, as model substrates, the minimum electrostatic potential of the alcohol substrate was located at the C_α-OH group (-31.50 kcal/mol), indicating its preferential activation site [Figure 3C]. After oxidation, the electrostatic potential minimum shifted to the C_α = O group with a significantly more negative value (-41.61 kcal/mol), revealing pronounced electronic redistribution induced by carbonyl formation. To assess the involvement of ·O_2^- in C_α-OH oxidation, 1-phenylethanol was employed as a model

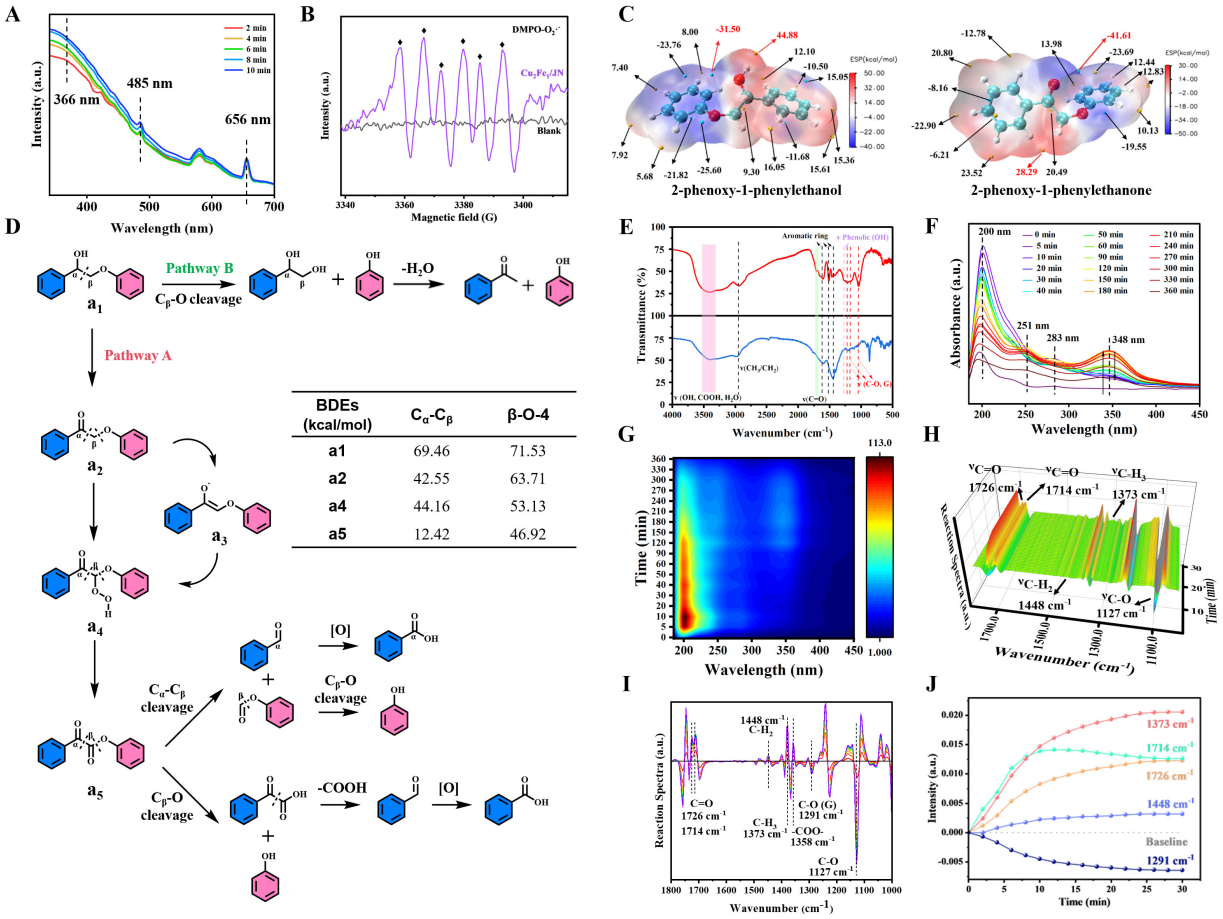

Figure 3. Mechanistic insights into ROS-mediated oxidative depolymerization of calcium lignosulfonate over Cu_2Fe_1/JN. (A) Time-dependent UV-vis spectra of TMB oxidation; (B) EPR spectra of DMPO-trapped ROS; (C) Molecular electrostatic potential surfaces of 2-phenoxy-1-phenylethanol and 2-phenoxy-1-phenylethanone; (D) Proposed catalytic oxidation pathway of 2-phenoxy-1-phenylethanol; (E) FTIR spectra of calcium lignosulfonate before oxidation (upper) and after oxidation (lower); (F and G) Time-dependent UV-vis spectra of calcium lignosulfonate during oxidative depolymerization and the corresponding 2D contour plot; (H and I) Three-dimensional FTIR spectra of calcium lignosulfonate during oxidative depolymerization, and the corresponding 2D plot; (J) The profiles of five selected characteristic peaks (the signal intensities were directly obtained from the instrument and exported for plotting). BDE: Bond dissociation energy; ROS: reactive oxygen species; TMB: 3,3′,5,5′-tetramethylbenzidine; EPR: electron paramagnetic resonance; DMPO: 5,5′-dimethyl-1-pyrroline *N*-oxide; FTIR: Fourier-transform infrared.

Table 1. ROS trapping results for the oxidation of 2-phenoxy-1-phenylethanol

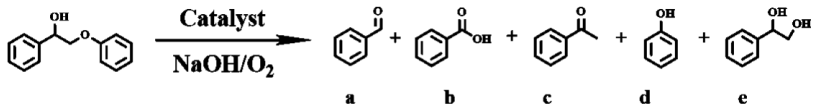

Entry	Trapping agent	Target ROS	Conv. (%)	Products yield (%)				
				a	b	c	d	e
1	-	-	99.1	56.3	32.0	0.6	0.02	0.01
2	isopropanol	·OH	99.0	58.0	30.1	0.5	0.03	0.02
3	β-carotene	$^1O_2$	99.1	55.2	29.8	0.5	0.04	0.02
4	*p*-benzoquinone	$\cdot O_2^-$	56.1	18.4	10.0	0.4	0.03	0.01

ROS: Reactive oxygen species.

Table 2. Product analysis and ROS trapping results for the oxidation of 1-phenylethanol

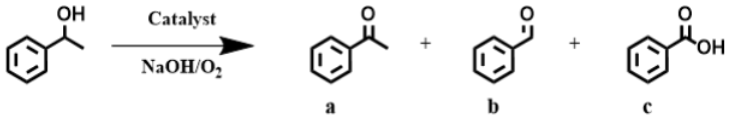

Entry	Time (h)	Conv. (%)	Product yield (%)		
			a	b	c
1	1	45.7	5.2	25.6	0.0
2	2	68.2	19.6	29.5	2.6
3	3	82.1	25.0	30.5	9.3
4	4	91.4	26.6	18.8	24.4
5	5	96.5	25.6	14.8	37.4
6a	5	48.4	0.0	17.8	3.6

[a]Control experiment using *p*-benzoquinone as a radical trapping agent. ROS: Reactive oxygen species.

substrate [Table 2]. Substrate conversion increased from 45.7% to 96.5% over 1-5 h, accompanied by an initial accumulation of acetophenone (from 5.2% at 1 h to 26.6% at 4 h) followed by a slight decline (25.6% at 5 h). Benzaldehyde showed a similar transient profile, whereas benzoic acid accumulated progressively to 37.4% at 5 h. Addition of *p*-benzoquinone markedly suppressed the formation of acetophenone, benzaldehyde, and benzoic acid to 0.0%, 17.8%, and 3.6%, respectively. Together with the EPR results, these observations support the involvement of $\cdot O_2^-$ in C_α-OH oxidation and subsequent carbonyl formation.

To further elucidate the oxidative cleavage of 2-phenoxy-1-phenylethanol, the bond dissociation energies (BDEs) of the C_α-C_β and β-O-4 bonds along the reaction pathways were calculated [Figure 3D]. In 2-phenoxy-1-phenylethanol (**a1**), the BDEs of the C_α-C_β and β-O-4 bonds were 69.46 and 71.53 kcal/mol, respectively. Upon formation of the carbonyl intermediate (**a2**), $\cdot O_2^-$ attacked **a2** to generate the intermediate **a3**, which subsequently evolved into the peroxy intermediate (**a4**). This process substantially lowered the corresponding BDEs of the C_α-C_β and β-O-4 bonds to 44.16 and 53.13 kcal/mol, respectively. Owing to the intrinsic instability of **a4**, homolytic cleavage of the O-O bond yielded 2-oxo-2-phenylacetate phenyl ester (**a5**), accompanied by a further drastic decrease in the BDEs of the C_α-C_β and β-O-4 bonds to only 12.42 and 46.92 kcal/mol, respectively. Subsequent bond cleavage and oxidation ultimately afforded phenol and benzoic acid (**Pathway A**). In contrast, thermal activation could induce direct cleavage of the C_β-O-4 bond in **a1**, producing phenylethane-1,2-diol and phenol (**Pathway B**), with the diol subsequently undergoing dehydration to form acetophenone. However, the yields of phenylethane-1,2-diol and acetophenone were low (0.01% and 0.6%, respectively), whereas benzaldehyde and benzoic acid reached yields of 56.3% and 32.0%, respectively [Table 1]. These results strongly support **Pathway A** as the dominant route, in which $\cdot O_2^-$-mediated pre-oxidation of the C_α-OH group to the carbonyl intermediate markedly weakens both the C_α-C_β and β-O-4 bonds, thereby facilitating their subsequent cleavage. Notably, although phenol is an expected product, its detected yield was only 0.02% [Table 1], likely owing to the high susceptibility of phenol to oxidation.

The structural evolution of calcium lignosulfonate before and after oxidation was further examined by FTIR spectroscopy [Figure 3E]. After catalytic oxidation, the characteristic bands at approximately 3,400, 2,934, and 1,700-1,750 cm^{-1}, assigned to O-H stretching, aliphatic C-H stretching, and C=O stretching vibrations, respectively, were significantly weakened[52-54]. This attenuation reflects hydroxyl group consumption and oxidation of the lignosulfonate side chains. Meanwhile, the decreased intensities of the bands at 1,271 and 1,211 cm^{-1}, corresponding to Ar-O-C stretching and C-O vibrations in guaiacyl (G) units, respectively,

indicate the disruption of G-type lignin structures during oxidation. Combined with the identification of vanillin, acetovanillone, and vanillic acid as major products, these results support the formation of G-derived aromatic monomers through cleavage and oxidation of lignin fragments. To capture the dynamic structural evolution during depolymerization, *in situ* UV-vis spectroscopy was employed to monitor changes in aromatic structures and functional groups throughout the reaction [Figure 3F and G]. The absorption shoulder at approximately 251 nm, associated with free and etherified -OH groups in calcium lignosulfonate, gradually increased during the initial reaction stage[55], suggesting the formation of new phenolic structures through ether bond cleavage. Meanwhile, the band centered at approximately 283 nm, originating from $\pi \rightarrow \pi$ transitions of aromatic structures containing conjugated C_α=C_β units and $n \rightarrow \pi$ transitions of carbonyl-containing aromatics[56,57], exhibited a similar increase within the first 3 h. These changes indicate the progressive fragmentation of calcium lignosulfonate macromolecules and the generation of low-molecular-weight aromatic intermediates with enhanced conjugation. In parallel, the continuous growth of the absorption band at ~348 nm, assigned to $n \rightarrow \pi$ transitions of carbonyl groups[58], implies the accumulation of oxygenated aromatic species, including aldehydes, ketones, and carboxylic acids. After prolonged oxidation (> 3 h), the gradual decrease in the absorption intensities of these aromatic and carbonyl-related bands suggests further oxidation and degradation of the products. According to product analysis, vanillin, acetovanillone, and vanillic acid are generated during calcium lignosulfonate depolymerization and likely undergo further oxidative transformation, potentially leading to ring-opening reactions and mineralization into CO_2 and H_2O[27]. In contrast, Cu/JN and Fe/JN showed only marginal spectral evolution throughout the reaction [Supplementary Figures 10 and 11], further underscoring the importance of Cu-Fe synergy in sustaining calcium lignosulfonate depolymerization and subsequent intermediates conversion. *In situ* FTIR measurements provided additional evidence for the progressive oxidation of calcium lignosulfonate structures [Figure 3H-J]. The continuous attenuation of the band at 1,127 cm^{-1}, attributed to Ar-O-C stretching vibrations[59], reflects the gradual disruption of the ether-linked C-O bond. Meanwhile, the enhanced signals at 1,373 and 1,714 cm^{-1} correspond to the formation of oxidized side-chain functionalities[27,59]. The increased intensity of the C-H bending vibration at 1448 cm^{-1} further indicates the transformation of aromatic side chains[60,61], consistent with the formation of aromatic ketone intermediates such as acetovanillone. Taken together, the radical-trapping experiments and time-dependent product evolution establish the involvement of $\cdot O_2^-$ and C_α-OH oxidation in the reaction sequence. The MEPS and BDE calculations further provide an electronic and energetic basis for the proposed C_α-OH oxidation and subsequent bond cleavage. Moreover, the FTIR and UV-vis measurements capture the accompanying structural evolution of lignosulfonate during depolymerization. Collectively, these complementary results support a ROS-mediated pathway involving C_α-OH oxidation, C_α-C_β and β-O-4 bond cleavage, formation of aromatic intermediates, and their subsequent oxidation. The synergistic Cu-Fe active centers enable efficient O_2 activation and selective cleavage of lignin linkages, thereby driving the depolymerization of lignin into valuable aromatic chemicals.

CONCLUSION

In summary, a mesoporous silica-supported Cu-Fe bimetallic catalyst (Cu_2Fe_1/JN) has been developed for selective oxidative depolymerization of calcium lignosulfonate. The optimized Cu-Fe species enabled efficient O_2 activation and selective generation of $\bullet O_2^-$ through coupled Cu^+/Cu^{2+} and Fe^{2+}/Fe^{3+} redox cycles, achieving 71.8% recovery of G-type aromatic monomers based on the NBO-estimated theoretical yield. Mechanistic studies revealed that $\bullet O_2^-$ initiates C_α-OH oxidation to form carbonyl intermediates, which promotes C_α-C_β and β-O-4 bond cleavage while minimizing over-oxidation of aromatic products. This work highlights the importance of interfacial electronic regulation in controlling ROS evolution and provides a rational strategy for designing selective oxidation catalysts for lignin valorization.

DECLARATIONS

Acknowledgements

The authors thank Xiyue Ma (Ceshihui Lab, www.ceshihui.cn) for assistance with the EPR test, and Xinyue Wang (Shiyanjia Lab, www.shiyanjia.com) for assistance with the XPS test. The authors also sincerely thank Professor James H. Clark from the University of York for revising and polishing the language throughout the manuscript.

Authors' contributions

Methodology: Gao, J.; Liu, J.
Funding acquisition: Gao, J.; Zhang, S.
Writing-original draft: Gao, J.; Li, L.
Writing-review & editing: Gao, J.; Cao, Y.; Guo, Y.; Mao, H.; Zhang, S.
Investigation: Cai, Y.; Li, J.
Formal analysis: Cai, Y.; Li, L.; Li, J.; Cao, Y.; Guo, Y.; Zhang, P.; Mo, L.; Zhou, A.; Liu, J.
Visualization: Cai, Y.; Li, J.; Zheng, X.; Mo, L.; Zhou, A.
Data curation: Cao, Y.; Zhang, P.; Zheng, X.
Supervision: Liu, J.; Mao, H.; Zhang, S.
Conceptualization: Mao, H.
Resources: Mao, H.

Availability of data and materials

The original contributions presented in this study are included in the article/Supplementary Materials. Please direct further inquiries to the corresponding authors.

AI and AI-assisted tools Statement.

Not applicable.

Financial support and sponsorship

This work was supported by the Collaborative Innovation Center of Fragrance Flavour and Cosmetics (1021ZK250028008-A06) and the National Natural Science Foundation of China (No. 22278085).

Conflicts of interest

Mo, L. and Zhou, A. are affiliated with Jiaxing Zhonghua Chemical Co., Ltd., while the other authors declare there are no conflicts of interest.

Ethical approval and consent to participate.

Not applicable.

Consent for publication

Not applicable.

Supplementary Materials

Supplementary Materials

REFERENCES

1. Sun, Z.; Fridrich, B.; de, Santi. A.; Elangovan, S.; Barta, K. Bright side of lignin depolymerization: toward new platform chemicals. *Chem. Rev.* **2018**, *118*, 614-78. DOI PubMed PMC
2. Zhang, X.; Liu, Z.; Li, B.; Yuan, Y. Tapping into the natural aromatic potential of microbial lignin valorization towards aromatic fine chemicals. *Green. Chem.* **2024**, *26*, 11378-405. DOI
3. Daelemans, B.; Sridharan, B.; Jusner, P.; et al. From lignin to market: a technical and economic perspective of reductive depolymerization approaches. *Green. Chem.* **2025**, *27*, 13160-78. DOI

4. Wang, S.; Li, X.; Ma, R.; Song, G. Catalytic Hydrogenolysis of lignin into serviceable products. *Acc. Chem. Res.* **2025**, *58*, 529-42. DOI
5. Zhuang, Y.; Dong, Y.; Zheng, Y.; Zhang, W.; Dong, L.; Chen, Z. Engineering oxygen vacancies on ceria *via* vanadium oxide dispersion for selective photocatalytic cleavage of lignin C-C bonds. *Green. Chem.* **2026**, *28*, 471-82. DOI
6. Fu, N.; Liu, R.; Zhou, Y.; Li, B.; Yuan, Y.; Liu, Z. Technological advances in ligninolytic enzymes for the biological valorization of lignin. *Green. Chem.* **2025**, *27*, 4016-39. DOI
7. Jiang, W.; Li, Q.; Cao, M.; Lou, H.; Li, Z.; Qiu, X. High-efficiency dual-site biomimetic catalyst for lignin depolymerization. *ACS. Catal.* **2025**, *15*, 2595-606. DOI
8. Kaur, P.; Wang, J.; Li, X.; et al. Valorization of lignin and its derived molecules by electrocatalytic oxidation. *ACS. Sustain. Chem. Eng.* **2025**, *13*, 16214-31. DOI PubMed PMC
9. Qin, Z.; Lakra, A.; Somni, R. R.; et al. A robust atomically precise nanocluster catalyst for simultaneous C-O and C-C bond cleavage in lignin models. *ACS. Catal.* **2025**, *15*, 20270-83. DOI PubMed PMC
10. Tan, F. F. Photocatalytic valorization of lignin: radical-mediated scission of recalcitrant bonds to aromatics. *RSC. Adv.* **2025**, *15*, 21947-61. DOI PubMed PMC
11. Zhang, J.; Bai, W.; Xu, J.; et al. The crucial role of oxygen evolution reaction in electrocatalytic oxidative C-C bond cleavage in lignin biomass valorization. *Angew. Chem. Int. Ed. Engl.* **2025**, *64*, e202510437. DOI
12. Cao, J.; Chen, X.; Yan, K.; Liu, H.; Shi, J.; Li, N. Native lignin isolation facilitated by cellulase desorption. *ACS. Sustainable. Chem. Eng.* **2025**, *13*, 6286-96. DOI
13. Hayashi, T.; Ishikawa, A.; Hosoya, T.; Miyafuji, H. Guaiacylglycerol as an intermediate in vanillin production during oxidative conversion of guaiacyl lignin under alkaline conditions. *Eur. J. Org. Chem.* **2025**, *28*, e202401272. DOI
14. Abdelaziz, O. Y.; Clemmensen, I.; Meier, S.; et al. On the oxidative valorization of lignin to high-value chemicals: a critical review of opportunities and challenges. *ChemSusChem* **2022**, *15*, e202201232. DOI PubMed PMC
15. Schupp, N.; Rücker, T.; Glöckner, E.; Wittgens, B.; Waldvogel, S. R. Highly concentrated peroxodicarbonate for efficient oxidative degradation of kraft lignin. *ChemSusChem* **2025**, *18*, e202500741. DOI PubMed PMC
16. Hafezisefat, P.; Lindstrom, J. K.; Brown, R. C.; Qi, L. Non-catalytic oxidative depolymerization of lignin in perfluorodecalin to produce phenolic monomers. *Green. Chem.* **2020**, *22*, 6567-78. DOI
17. Garedew, M.; Lam, C. H.; Petitjean, L.; et al. Electrochemical upgrading of depolymerized lignin: a review of model compound studies. *Green. Chem.* **2021**, *23*, 2868-99. DOI
18. Cheng, X.; Palma, B.; Zhao, H.; et al. Photoreforming for lignin upgrading: a critical review. *ChemSusChem* **2023**, *16*, e202300675. DOI
19. Aboagye, D.; Djellabi, R.; Medina, F.; Contreras, S. Radical-mediated photocatalysis for lignocellulosic biomass conversion into value-added chemicals and hydrogen: facts, opportunities and challenges. *Angew. Chem. Int. Ed. Engl.* **2023**, *62*, e202301909. DOI PubMed
20. Ha, J.; Kang, J.; Lim, S. H.; Cho, D. W.; Oh, K. I.; Kim, Y. Water-accelerated photooxidation and degradation of lignin linkages mediated by plasmonic catalysts. *Chem. Sci.* **2025**, *16*, 9447-53. DOI PubMed PMC
21. Tian, J.; Wu, J.; Lin, F.; Ma, Y.; Sun, Y. Defect engineering-regulated electron transfer of NiAl-MMO for catalyzing directed conversion of lignin into cyclohexanol-based chemicals. *ACS. Sustainable. Chem. Eng.* **2025**, *13*, 16884-96. DOI
22. Zhang, J.; Ge, Y.; Li, Z. Synergistic magnetic Cu-Fe catalysts on N-doped biochar for efficient alkali lignin catalytic depolymerization into monophenols. *Ind. Crop. Prod.* **2024**, *222*, 119663. DOI
23. Li, L.; Kong, J.; Long, J.; et al. Hierarchical hollow silicalite encapsulated Cu-Fe oxides for selectively oxidative depolymerization of lignin to diethyl meleate. *J. Catal.* **2025**, *448*, 116157. DOI
24. Zhang, Z.; Han, P.; Li, L.; et al. Confinement-enhanced selective oxidation of lignin derivatives to formic acid over Fe-Cu/ZSM-5 catalysts under mild conditions. *ChemSusChem* **2022**, *15*, e202200218. DOI
25. Gao, P.; Su, Y.; Xie, Y.; Wang, J.; Zeng, G.; Sun, D. A systematic review on persulfate activation induced by functionalized mesoporous silica catalysts for water purification. *Sustainability* **2025**, *17*, 9199. DOI
26. Jankowska, A.; Kowalczyk, A.; Rutkowska, M.; Michalik, M.; Chmielarz, L. Catalytic performance of bimetallic systems (Cu-Fe, Cu-Mn, Fe-Mn) based on spherical MCM-41 modified by template ion-exchange in NH_3-SCR process. *Catalysts* **2022**, *12*, 885. DOI
27. Liu, J.; Li, J.; Zhu, Z.; et al. Selective oxidation of lignin to aromatic aldehydes and ketones over a spinel Cu-Mn catalyst supported on layered double oxides. *Appl. Catal. B-Environ.* **2026**, *383*, 126033. DOI
28. Hehre, W. J.; Ditchfield, R.; Pople, J. A. Self - consistent molecular orbital methods. XII. further extensions of gaussian - type basis sets for use in molecular orbital studies of organic molecules. *J. Chem. Phys.* **1972**, *56*, 2257-61. DOI
29. Dasireddy, V. D. B. C.; Bharuth-Ram, K.; Hanzel, D.; Likozar, B. Heterogeneous Cu-Fe oxide catalysts for preferential CO oxidation (PROX) in H_2-rich process streams. *RSC. Adv.* **2020**, *10*, 35792-802. DOI PubMed PMC
30. Zou, Z.; Shen, Y.; Chen, C.; et al. Size-controlled Ni nanoparticles confined into amino-modified mesoporous silica for efficient hydrodeoxygenation of bio-derived aromatic aldehyde. *Adv. Funct. Mater.* **2025**, *35*, 2417584. DOI

31. Guan, X.; Han, R.; Asakura, H.; et al. Designing reactive bridging O^{2-} at the atomic Cu-O-Fe site for selective NH_3 oxidation. *ACS. Catal.* **2022**, *12*, 15207-17. DOI PubMed PMC
32. Hu, Y.; Zhou, Y.; Ding, R.; et al. Sustainable Fe and Cu sites double redox cycle boosting Fenton-like degradation of organic pollutants. *Environ. Sci. Technol.* **2025**, *59*, 16812-21. DOI
33. Mi, J.; Lan, Z.; Chen, J.; Cao, Y.; Jiang, L. MgAl-LDO mixed oxide derived from layered double hydroxide: a potential support for CoMo sulfur-resistant water-gas shift catalyst. *Catal. Commun.* **2016**, *78*, 44-7. DOI
34. Li, J.; Zheng, M.; Wei, F.; et al. Fe doped $InVO_4$ nanosheets with rich surface oxygen vacancies for enhanced electrochemical nitrogen fixation. *Chem. Eng. J.* **2022**, *431*, 133383. DOI
35. Wang, K.; Yu, Q.; Qin, Q. Reduction kinetics of cu-based oxygen carriers for chemical looping air separation. *Energy. Fuels.* **2013**, *27*, 5466-74. DOI
36. Fukushima, J.; Takizawa, H. *In situ* spectroscopic analysis of the carbothermal reduction process of iron oxides during microwave irradiation. *Metals* **2018**, *8*, 49. DOI
37. Tan, S.; Hu, B.; Kim, W.; et al. Propane dehydrogenation over alumina-supported iron/phosphorus catalysts: structural evolution of iron species leading to high activity and propylene selectivity. *ACS. Catalysis.* **2016**, *6*, 5673-83. DOI
38. Dong, L.; Lin, L.; Han, X.; et al. Breaking the limit of lignin monomer production via cleavage of interunit carbon-carbon linkages. *Chem* **2019**, *5*, 1521-36. DOI
39. Jeon, W.; Choi, I.; Park, J.; Lee, J.; Hwang, K. Alkaline wet oxidation of lignin over Cu-Mn mixed oxide catalysts for production of vanillin. *Catal. Today.* **2020**, *352*, 95-103. DOI
40. Schutyser, W.; Renders, T.; Van, den. Bosch. S.; Koelewijn, S. F.; Beckham, G. T.; Sels, B. F. Chemicals from lignin: an interplay of lignocellulose fractionation, depolymerisation, and upgrading. *Chem. Soc. Rev.* **2018**, *47*, 852-908. DOI PubMed
41. Fache, M.; Boutevin, B.; Caillol, S. Vanillin production from lignin and its use as a renewable chemical. *ACS. Sustainable. Chem. Eng.* **2016**, *4*, 35-46. DOI
42. Zhu, Y.; Liao, Y.; Lv, W.; et al. Complementing vanillin and cellulose production by oxidation of lignocellulose with stirring control. *ACS. Sustainable. Chem. Eng.* **2020**, *8*, 2361-74. DOI
43. Zhu, Y.; Liu, J.; Liao, Y.; Lv, W.; Ma, L.; Wang, C. Degradation of vanillin during lignin valorization under alkaline oxidation. *Top. Curr. Chem. (Cham).* **2018**, *376*, 29. DOI
44. Fargues, C.; Mathias, Á.; Silva, J.; Rodrigues, A. Kinetics of vanillin oxidation. *Chem. Eng. . Technol.* **1996**, *19*, 127-36. DOI
45. Guo, H.; Miles-Barrett, D. M.; Neal, A. R.; Zhang, T.; Li, C.; Westwood, N. J. Unravelling the enigma of lignin(OX): can the oxidation of lignin be controlled? *Chem. Sci.* **2018**, *9*, 702-11. DOI PubMed PMC
46. Ma, C.; Zhang, J.; Yin, Y.; Suo, C.; Liu, S. Free radical theory in lignin oxidation depolymerization. *Trends. Chem.* **2024**, *6*, 234-47. DOI
47. Yuan, J.; Li, H.; Xiao, L.; et al. Valorization of lignin into phenolic compounds via fast pyrolysis: Impact of lignin structure. *Fuel* **2022**, *319*, 123758. DOI
48. Bains, R.; Kumar, M.; Chauhan, A. S.; Kumar, A.; Das, P. Synthetic approach for the oxidative depolymerization of biomass-derived lignin to vanillin, vanillic acid, and acetovanillone compounds. *Bioresour. Technol. Rep.* **2026**, *34*, 102676. DOI
49. Sun, Y.; Liu, H.; Tan, X.; et al. Highly efficient redox reaction between potassium permanganate and 3,3',5,5'-tetramethylbenzidine for application in hydrogen peroxide based colorimetric assays. *RSC. Adv.* **2019**, *9*, 1889-94. DOI PubMed PMC
50. Yang, W.; Zhu, Y.; You, F.; et al. Insights into the surface-defect dependence of molecular oxygen activation over birnessite-type MnO_2. *Appl. Catal. B. Environ.* **2018**, *233*, 184-93. DOI
51. Hu, Y.; Yan, L.; Zhao, X.; et al. Mild selective oxidative cleavage of lignin C-C bonds over a copper catalyst in water. *Green. Chem.* **2021**, *23*, 7030-40. DOI
52. Cao, Y.; Gao, J.; Zhang, C.; et al. Fast and selective production of aromatics via efficient lignin depolymerization: critical factors and mechanism studies. *ACS. Sustainable. Chem. Eng.* **2022**, *10*, 15273-83. DOI
53. Qu, R.; Zhang, W.; Liu, N.; et al. Antioil Ag_3PO_4 nanoparticle/polydopamine/Al_2O_3 sandwich structure for complex wastewater treatment: dynamic catalysis under natural light. *ACS. Sustainable. Chem. Eng.* **2018**, *6*, 8019-28. DOI
54. Malik, M. A.; Surepally, R.; Akula, N.; Cheedarala, R. K.; Alshehri, A. A.; Alzahrani, K. A. Oxidation of alcohols into carbonyl compounds using a CuO@GO nano catalyst in oxygen atmospheres. *Catalysts* **2023**, *13*, 55. DOI
55. Passauer, L.; Salzwedel, K.; Struch, M.; Herold, N.; Appelt, J. Quantitative analysis of the etherification degree of phenolic hydroxyl groups in oxyethylated lignins: correlation of selective aminolysis with FTIR spectroscopy. *ACS. Sustainable. Chem. Eng.* **2016**, *4*, 6629-37. DOI
56. Zirbes, M.; Graßl, T.; Neuber, R.; Waldvogel, S. R. Peroxodicarbonate as a green oxidizer for the selective degradation of kraft lignin into vanillin. *Angew. Chem. Int. Ed. Engl.* **2023**, *62*, e202219217. DOI

57. Hynynen, J.; Riddell, A.; Achour, A.; et al. 'Lignin and extractives first' conversion of lignocellulosic residual streams using UV light from LEDs. *Green. Chem.* **2021**, *23*, 8251-9. DOI
58. Salthammer, T. Analytical chemistry of carbonyl compounds in indoor air. *Analyst* **2023**, *148*, 3432-51. DOI PubMed
59. Vizintin, A.; Bitenc, J.; Kopač, Lautar. A.; et al. Probing electrochemical reactions in organic cathode materials via in operando infrared spectroscopy. *Nat. Commun.* **2018**, *9*, 661. DOI PubMed PMC
60. Khalili, K. N. M.; de, Peinder. P.; Donkers, J.; Gosselink, R. J. A.; Bruijnincx, P. C. A.; Weckhuysen, B. M. Monitoring molecular weight changes during technical lignin depolymerization by operando attenuated total reflectance infrared spectroscopy and chemometrics. *ChemSusChem* **2021**, *14*, 5517-24. DOI PubMed PMC
61. Riddell, L. A.; de, Peinder. P.; Polizzi, V.; Vanbroekhoven, K.; Meirer, F.; Bruijnincx, P. C. A. Predicting molecular weight characteristics of reductively depolymerized lignins by ATR-FTIR and chemometrics. *ACS. Sustain. Chem. Eng.* **2024**, *12*, 8968-77. DOI PubMed PMC